ACS APPLIED MATERIALS & INTERFACES

Research Article

www.acsami.org

Inkjet Printing of Sol–Gel Synthesized Hydrated Tungsten Oxide Nanoparticles for Flexible Electrochromic Devices

Cláudia Costa,[†,‡] Carlos Pinheiro,[§] Inês Henriques,[§] and César A. T. Laia*[,‡]

[†]YDreams, Madan Parque–Sul, 2825-149 Caparica, Portugal

[‡]Requimte, Departamento de Química, Faculdade de Ciências e Tecnologia, Universidade Nova de Lisboa, 2829-516 Caparica, Portugal.

[§]Ynvisible, Rua Mouzinho de Albuquerque 7, 2070-104 Cartaxo, Portugal

Supporting Information

ABSTRACT: Tungsten oxide nanoparticles were synthesized via a sol–gel route using metallic tungsten as precursor, and were printed on a flexible electrode using inkjet printing in order to build solid-state electrochromic cells. Several spectroscopic techniques were used to characterize and compare tungsten oxide particles obtained from different origins. FTIR, Raman and X-ray diffraction spectroscopic measurements showed that the sol–gel synthesis described here produces nanoparticles mainly in an amorphous state with hexagonal crystalline domains and allowed the analysis of the hydration extent of those nanoparticles. The size was measured combining dynamic light scattering, sedimentation, and microscopic techniques (AFM), showing a consistent size of about 200 nm. The tungsten oxide nanoparticles were used to produce an ink formulation for application in inkjet printing. Solid-state electrochromic devices were assembled at room temperature, without sintering the tungsten oxide printed films, showing excellent contrast between on/off states. Electrochemical characterization of those films is described using cyclic voltammetry. The devices were then tested through spectroelectrochemistry by Visible/NIR absorption spectroscopy (400–2200 nm range), showing a dual spectroscopic response depending on the applied voltage. This phenomenon is attributed to the presence of two different crystalline states in accordance with results obtained from the spectroscopic characterization of the nanoparticles. The electrochromic cells had a good cycling stability showing high reversibility and a cyclability up to more than 50 000 cycles with a degradation of 25%.

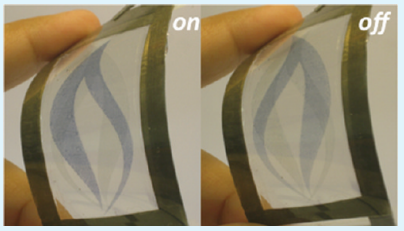

KEYWORDS: *inkjet printing, tungsten trioxide, electrochromic devices, nanoparticles, electrochromism*

1. INTRODUCTION

Printed electronics has attracted the attention from both Academia and Industry, mainly because of potential applications in everyday life by introducing electronic devices on common substrates (e.g., plastic foils or paper).[1] The fundamental idea behind printed electronics is to construct electronic devices and components on which transistors,[2] light-emitting devices[3] or electrochromic cells[4] can be integrated through roll-to-roll printing methods. The objective is to construct flexible devices, so that they can be used as inexpensive electronic components using accessible production methods. In this context, inkjet printing plays an important role, and indeed there are a number of publications using it to build conductive layers, transistors, and light emitting devices.[2,3,5−12] Electrochromic cells can also be built using this deposition method.[4,10]

In electrochromism, the active materials can be organic molecules, such as viologens[13] and leuco dyes,[14] semiconductor polymers, such as PEDOT,[13,15] or metal oxides, such as WO_3. WO_3 is, perhaps, one of the most well-known electrochromic substances. Its application is well reviewed in several books and papers,[13,16−19] and, along with viologens, it has been commercially explored on electrochromic applications such as "intelligent windows".[20−23] WO_3 popularity stems from its strong color contrast with a relatively low production cost. WO_3 has transitions both in the near-infrared and visible region of the light spectrum, filtering thus an important part of the solar light and potentially reducing air-conditioning costs in buildings (thus justifying its application on intelligent windows). The usual deposition method for WO_3 is sputtering, and much of the literature and technological applications apply this technique.[17,24−39]

To use other methods, such as inkjet printing, it is important to synthesize the compound as nanoparticles, which can be achieved using a sol–gel method,[16,21,40−54] because larger particles may damage the printer nozzles. Normally, in this case, amorphous tungsten oxide nanoparticles are obtained,[21,41,43−47,49,50] which can be followed by a thermal sintering process in order to make crystalline nanoparticles or coatings. Such treatment, however, is not compatible with heat sensitive substrates such as plastic or paper, and therefore the applicability of this electrochromic material on flexible printed

Received: November 17, 2011
Accepted: February 9, 2012
Published: February 9, 2012

electronics is greatly reduced. We propose here a method in which tungsten oxide nanoparticles are synthesized via a sol−gel route and deposited afterward on a flexible electrode using inkjet printing without the sintering step. The nanoparticles and the coating obtained by inkjet printing are characterized using several different techniques. Spectroelectrochemical measurements show the electrochromic activity of the solid-state cells obtained, where optical activity occurs not only on the visible portion of the spectrum, but also in the near-infrared (NIR) region. Combining all different results, it is possible to assign two different crystalline states for tungsten oxide that give distinct electrochromic responses. The samples have high cyclability.

2. EXPERIMENTAL SECTION

2.1. Reagents. The following reagents were purchased and used without further purification: metallic tungsten (99.9%, Aldrich), hydrogen peroxide (30%, Fluka), tungsten(VI) oxide (99.9%, Fluka), acetonitrile (99.97%, Scharlau), and lithium perchlorate (98%, Aldrich). The electrolyte layer was prepared from a mixture containing a polyethylene oxide-polypropylene oxide copolymer (PEO-PPO). This copolymer has an average molecular weight of 150 000 D, and the fraction of PPO is 1% of the weight. The copolymer was dissolved in acetonitrile containing $LiClO_4$. The mass percentages were 24% for the copolymer, 12% for $LiClO_4$, and 64% for acetonitrile. Indium tin oxide (ITO)-coated PET (polyethylene terephthalate) with a surface resistivity of 60 Ω/sq was purchased from Sigma-Aldrich and used as received.

2.2. Tungsten Oxide Nanoparticle Synthesis. Metallic tungsten was added to hydrogen peroxide (6.8% (w/w) of metallic tungsten in hydrogen peroxide) and allowed to react about 3 min until a clear transparent colorless solution was formed (without aging or heating). This solution was heated (100 °C) under stirring in a closed vessel, giving a yellow solution after 2 h. A pale yellow precipitate appears after 5 h under the same conditions. The resulting dry powder was obtained after solvent evaporation and was characterized using the experimental techniques described below, confirming the presence of tungsten oxide nanoparticles. The composition of the powder was studied using X-ray fluorescence (XRF) and elemental analysis techniques. XRF measurements were performed in an ArtTAX spectrometer of Intax GmbH, with a molybdenum (Mo) anode, Xflash detector refrigerated by Peltier effect (Sidrift), with a mobile arm. The experimental parameters used were: 40 kV of voltage, 300 μA of intensity, for 200 s. Two XRF spectra were made, one for the synthesized powder and another using commercially available tungsten oxide powder (see reagents). The two spectra aligned perfectly, showing that there was no other element (heavier than oxygen) in the composition of the two powders.

Elemental analysis was performed in an elemental analyzer (Thermo Finnigan-CE Instruments, Italy, model Flash EA 1112 CHNS series). Again, a comparison with commercially available WO_3 powder was performed to determine differences in terms of percentage of carbon and hydrogen elements. The carbon percentage was practically the same (0.22% for the sol−gel powder and 0.24% for the commercial powder) in both samples. In the sol−gel powder, however, hydrogen was also detected (0.64%), whereas it was undetectable on the commercial powder.

To obtain lyophilized powder, we used an aqueous dispersion of the powder described. The sintered powder was obtained using the powder described and heating it at 550 °C for 2 h.

2.3. Inkjet. The obtained tungsten oxide nanoparticles were dispersed in water, giving a stable colloidal suspension characterized by sedimentation techniques. The ink dispersion used has a tungsten oxide concentration equal to 1.7 g/dm^3 in water. This ink has a surface tension equal to 65.4 mN/m, viscosity equal to 2.0 cP, density equal to 1.004 g/cm^3 and pH 4.0. Those ink physical properties are important to achieve an optimal printing performance, but they are not limitative. It is possible to print inks even if those values are outside the optimal ranges, but the reliability and drop formation maybe affected.

Drop-on-demand piezo (DOD piezo) lab-scale Dimatix materials printer (DMP-2800)) was used to print the tungsten oxide layer of the electrochromic devices. The optimal ink physical properties for this printer are: surface tension between 28−33 mN/m, viscosity between 3−12 cP, density above 1 g/cm^3 and pH between 4 and 8. The tungsten oxide ink was printed on top of the TCO (transparent conductive oxide) of the PET/ITO substrate (Figure 1). The ink was

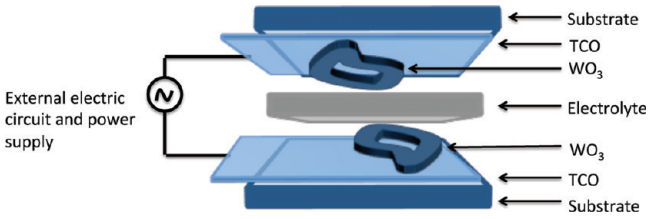

Figure 1. Scheme of the solid-state electrochromic device architecture used in this work. The substrate was PET coated with ITO.

printed using a waveform with an applied voltage of 14 V and a firing drop frequency of 6 kHz. The drops were small (volume equal to 10 pL, around 10 μm of radius) and spherical as required. A 20 μm drop spacing was employed. The reliability of the ink was 100% in 3 min of continuous printing (i.e., all the nozzles remained functional). Therefore, reliability and drop formation was maintained even though the ink physical properties were outside the optimal range described above.

2.4. Device Assembly. The architecture of the devices is shown in Figure 1, where both electrode and counter-electrode are tungsten oxide films deposited by inkjet printing. This architecture allows the measurement of light absorption between on and off states, because the patterns of the electrode and counter-electrode are different. Tungsten oxide was deposited by inkjet printing on top of the ITO layer. The lithium-based polymer electrolyte was spread-coated on top of one of the tungsten oxide layers and allowed to dry for 1 h. The device was closed and sealed.

2.5. Particle Characterization Techniques. *2.5.1. Dynamic Light Scattering (DLS) and Dispersion Analysis.* DLS experiments were performed on a Brookhaven Instruments BI-90, Brookhaven Instruments Corporation, New York. Speed, 1 min; accuracy, ±1%; sample volume, 0.5−3 mL were used. The mean particle size value and the standard deviation were calculated (size distribution by weight) assuming a Logonormal fit. The diffusion coefficient was measured for different sample concentrations and an extrapolation for infinite dilution was made. The particle size was determined using the Stokes−Einstein equation. The samples were previously filtered at 1 μm and 200 nm.

Ink sedimentation velocity and nanoparticles size were determined on different dispersions of sol−gel synthesized tungsten oxide nanoparticles, with a Lumisizer dispersion analyzer (LUM-GmbH, Germany). This apparatus allows acquisition of space- and time-resolved extinction profiles over the sample length. Parallel light (I_0) illuminates the entire sample cell and transmitted light (I) is detected by sensors arranged linearly across the sample from top to bottom. Transmission is converted into extinction coefficient and particle concentration is calculated, therefore allowing the sedimentation velocity to be determined. Centrifugal force is used to accelerate the sedimentation process. The equipment uses an indirect method to determine the nanoparticles size, using the density of the solid and the liquid phases, the liquid's viscosity and the sedimentation velocity, by applying Stokes law. Radial positions vs time were taken in order to calculate the sedimentation velocity for a given angular velocity, which afterward enables the particle diameter calculation. A plot of u vs $\omega^2 r/g$ (where g is the gravity acceleration constant) should give a straight line in which the slope is u for earth gravity.

2.5.2. X-ray Diffraction (XRD), Fourier Transform Infrared Spectroscopy (FTIR), and Raman Spectroscopy. XRD measurements were made on a powder X-ray diffractometer for powders, RIGAKU, model MiniFlex II, 30 kV/15 mA, with copper X-ray tubes. Infrared analyses were performed on a Nicolet Nexus spectrophotometer. Spectra were obtained in absorbance mode, with a resolution of 8 cm^{-1} and 64 scans. Spectra are shown here as acquired, without corrections or any further manipulation, except for baseline correction. The samples consisted of tungsten oxide powders grounded with potassium bromide. This powder mixture was then compressed in a mechanical press to form a translucent pellet through which the spectrophotometer infrared light beam passes. Raman spectroscopy was made in a Labram 300 JobinYvon spectrometer equipped with a He/Ne laser of 17 mW, operating at 632.8 nm and using the tungsten oxide powder.

2.5.3. Differential Scanning Calorimetry (DSC) and Thermogravimetric Analysis (TGA). DSC and TGA analysis were performed on the tungsten oxide nanoparticles powder with a Netzsch STA 409 PC Luxx. The scan temperature was between 40 and 1300 °C and the scan rate used was 10 °C/min.

2.6. Surface Tension and Viscosity Measurements. Ink surface tension was measured with a KSV Instruments Sigma 70 (Monroe, CT). The DuNoüy ring method was used (R = 9.545 mm, r = 0.185 mm and l = 119.9 mm) and the surface tension obtained value was corrected following the Zuidema-Waters method. The standard glass beaker had a 66 mm diameter and 110 mL maximum volume. The sample volume used was 80−100 mL. Five measurements were conducted for each sample. Ink viscosity measurements were made with a Brookfield LVT viscometer. Density was measured with a 25 mL pycnometer.

2.7. Electrochemical and Spectroelectrochemical Measurements. Electrochemical measurements on tungsten oxide inkjet printed films were performed in a conventional three-electrode cell. The tungsten oxide film deposited on an ITO electrode was the working electrode, a platinum wire was used as counter-electrode, a saturated calomel electrode (SCE) was the reference electrode and the supporting electrolyte was a polymer with lithium salt. For the solid-state electrochromic device a two-electrode cell configuration was used. The working electrode and the counter-electrode were both a layer of tungsten oxide film printed on the TCO, with the polymer electrolyte sandwiched between them, as described above (see Figure 1). The equipment used was a potentiostat/galvanostat Model 20 Autolab from Eco Chemie BV (Utrecht, The Netherlands). The collection of data was controlled by GPES version 4.9 Eco Chemie BV software. No IR compensation was used.

In situ UV/Vis absorbance spectra and chronoabsorptometry measurements of the tungsten oxide devices were performed using a UV−Vis−NIR spectrophotometer Varian Cary 5000 (spectral range from 220 to 3000 nm). The devices were potentiostatic or potentiodinamically controlled with a potenciostat/galvanostat model 20 Autolab as described as above. The two-electrode cell configuration is the same as above. The device was placed in the spectrophotometer compartment perpendicularly to the light beam. The potenciostat/galvanostat applied a square-waveform electric potential (at selected values described below), and the spectrophotometer registered the absorbance at the wavelengths selected for each experiment within the range of the equipment. Stability cycling tests were also performed in the same setup.

3. RESULTS AND DISCUSSION

3.1. Particle Size Determination and Sedimentation Measurements. Dynamic light scattering (DLS) measurements of the sol−gel tungsten oxide particles dispersions were done in water/ethanol mixtures 1:1 (v/v). This technique allows the determination of diffusion coefficients D, which can be afterward used to calculate the particle size. Samples with different volume fractions of dispersed phase (ϕ) were measured, allowing determination of D at each sample. It is known that extrapolations to infinite dilution are necessary to avoid interference of the attractive or repulsive forces between particles. This interference can be modeled by[55]

$$D = D_0(1 + \alpha\phi) \quad (1)$$

Where D_0 is the diffusion coefficient at infinite dilution and α is the virial coefficient. The virial coefficient provides information on the type of interactions that occur between nanoparticles. For hard spheres or when the interactions are repulsive because of electrostatic forces, α is positive, whereas when attractive interactions take place, the virial coefficient is negative.[55] Table 1 summarizes the values obtained from these experiments. The data shows that α is close to zero, meaning that repulsive and attractive interaction forces in this system are well balanced, canceling each other. Stokes−Einstein equation was then applied to calculate the average particle diameter d

Table 1. Values for the Diffusion Coefficient for Infinite Dilutions D_0, the Virial Coefficient α, and the Average Particle Diameter d, Obtained by DLS

	D_0 ($cm^2\ s^{-1}$)	α	d (nm)
filtration: 1 μm	$(9.7 \pm 0.1) \times 10^{-9}$	0 ± 0.1	230 ± 10
filtration: 200 nm	$(1.6 \pm 0.1) \times 10^{-8}$	0 ± 0.1	160 ± 10

$$d = \frac{k_B T}{3\pi\eta D_0} \quad (2)$$

Where k_B is the Boltzmann constant, T is the absolute temperature (298 K), and η is the solvent viscosity. The average particle diameters were in the range 160−225 nm, depending on the filtration used. As expected, the average diameters decrease slightly after filtration through a 200 nm filter.

Sedimentation velocity was determined by analytical centrifugation (see experimental section). This type of measurement relies on Stokes law (for particle diffusion under an acceleration field) and Lambert−Beer law (in order to convert optical transmission to particle concentration). Sedimentation velocity u depends on particle diameter, according to the following equation for diluted samples[56]

$$u = \frac{1}{18}\frac{\Delta\rho d^2}{\eta}\omega^2 r \quad (3)$$

where $\Delta\rho$ is the density difference between particles and the solvent, ω is the angular velocity and r is the radial position. $\omega^2 r$ represents the centrifugal acceleration experienced by the particles at each radial position. The profiles of optical transmission vs radial position vs time are obtained at different rotational speeds, and using Lambert−Beer law, it is possible to determine the sedimentation velocity for each angular velocity. In this work, a normalized optical transmission value was chosen in order to avoid meniscus and bottom cell errors.[57] This experimental value can then be compared with those calculated using the particle diameter obtained in DLS experiments, taking into account the solvent viscosity of each sample.

The sedimentation velocity is a measure of the stability of the inks. Therefore, an optimization of the ink formulation was done, by measuring u. Some of the data obtained are listed in the Supporting Information (Table S1). From this optimization, we arrived to the conclusion that the ink made from nanoparticles suspension in water, which was allowed to rest for 1 week, had a sedimentation velocity equal to 5.8 ± 0.1 mm/day

(filtration 1 μm). This is the formulation used in the rest of this work as the electrochromic ink, because it has a reasonable stability for the use as inkjet inks.

Because of the small nozzles size of common print heads (the nozzle size is typically around 20 μm for a 10 pl drop), inkjet formulations require particles with a size smaller than 1 μm.[58] This requirement excludes formulations with salt, because the particles aggregate rather easily in such conditions, or commercial tungsten oxide.

3.2. Thermal and Calorimetric Measurements. Figure 2 shows differential scanning calorimetry (DSC) and thermogravimetry analysis (TGA) of the synthesized sol–gel tungsten oxide nanoparticles, without sintering or lyophilization treatments. From the DSC results, a small exothermic crystallization peak is observed at 550 °C. Some other endothermic processes, around 100 °C and from 250 to 350 °C, seem also to take place, but their intensity is rather small. TGA analysis shows material loss in this region, thus these processes are most likely linked to solvent evaporation. An intense endothermic peak above 1200 °C is detected, without any significant mass change in TGA data, indicating a phase transition at this region (most probably the melting point, although for pure tungsten oxide it is reported to be 1473 °C. Such discrepancy could be due to the composition of the nanoparticles, see below). DSC measurements of other tungsten oxide materials discussed in this work are shown in the Supporting Information (Figure S1).

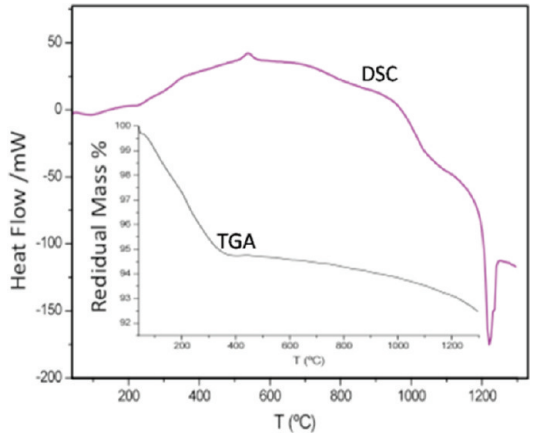

Figure 2. DSC and TGA analysis of the tungsten oxide synthesized nanoparticles (scan rate equal to 10 °C/min).

3.3. Particle Characterization by X-ray Diffraction (XRD), FTIR and Raman Spectroscopy. XRD, FTIR, and Raman spectroscopy were employed with the aim of characterizing the crystallinity of the synthesized powder. The DSC measurement clearly shows presence of solvent molecules (mainly water) and an exothermic crystallization peak at 550 °C. It is also known that sol–gel synthesized particles normally lead to the formation of amorphous material, which may be submitted to annealing after deposition to make crystalline particles (see references in the Introduction). The strategy consisted in analyzing four different tungsten oxide powders in order to make a comparison. In addition to the synthesized powder (A) and the commercially available tungsten oxide (B), two more powders were obtained: one in which A was sintered at 550 °C for 1 h (C) and another powder by dispersing A in water, followed by 1 week of aging and lyophilization, in order to obtain the "dry" powder D. Therefore, with powder C, we are able to characterize the crystallization process at 550 °C, whereas with powder D, the main objective was to check if dispersion and aging had an effect on the crystallinity of powder A. One must be aware, however, that the lyophilization treatment also can lead to changes in crystallinity, which will be further discussed below.

The XRD spectra (Figure 3) show well-defined diffraction peaks for all samples. However each sample displays different crystallinity. A (the synthesized particles) show peaks consistent with a hexagonal structure (JCPDS card 35–1001, hexagonal phase of $WO_3.0.33H_2O$) that indeed has some water molecules incorporated. As expected from the specifications of the supplier, B shows a cubic structure (JCPDS card 46–1096, cubic phase of WO_3) without presence of water molecules. C has a tetragonal structure (JCPDS card 53–0434, tetragonal phase of WO_3), different from B, but also without water molecules. This result confirms that at 550 °C, the solvent is removed and the particles change their crystallinity. Powder D displays an orthorhombic structure (JCPDS card 43–0679, orthorhombic phase of $WO_3.H_2O$). Finally XRD peaks of A and D suggest that probably an amorphous phase coexists with the crystalline phase (more broad and with less intensity peaks are obtained).

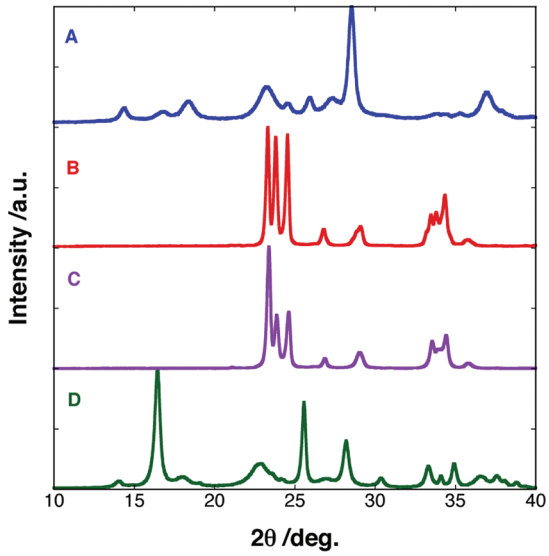

Figure 3. (A) XRD spectra of synthesized powder, (B) commercially available WO_3, (C) synthesized powder sintered at 550 °C for 1 h and (D) synthesized powder dispersed in water, followed by 1 week aging and lyophilization.

FTIR and Raman spectra can provide a more conclusive answer for the presence of an amorphous phase and/or hydration of tungsten oxide. Several revealing features are observed in this set of spectra (see Figure 4). At 3400 cm^{-1} and 1615 cm^{-1} intense absorption IR peaks are observed on powders A and D. These results were expected since they correspond to vibrational modes of water molecules. These peaks are almost absent on powders B and C. Powders A and D also display a transition at 946 cm^{-1}, with small intensity in FTIR spectra but more evident in the Raman spectra, which is attributed to W=O or terminal W–O in amorphous compounds.[52,59,60] Around 820 cm^{-1} every sample displays a transition which relative intensity depends on the powder. These transitions are attributed to the W–O stretching mode,

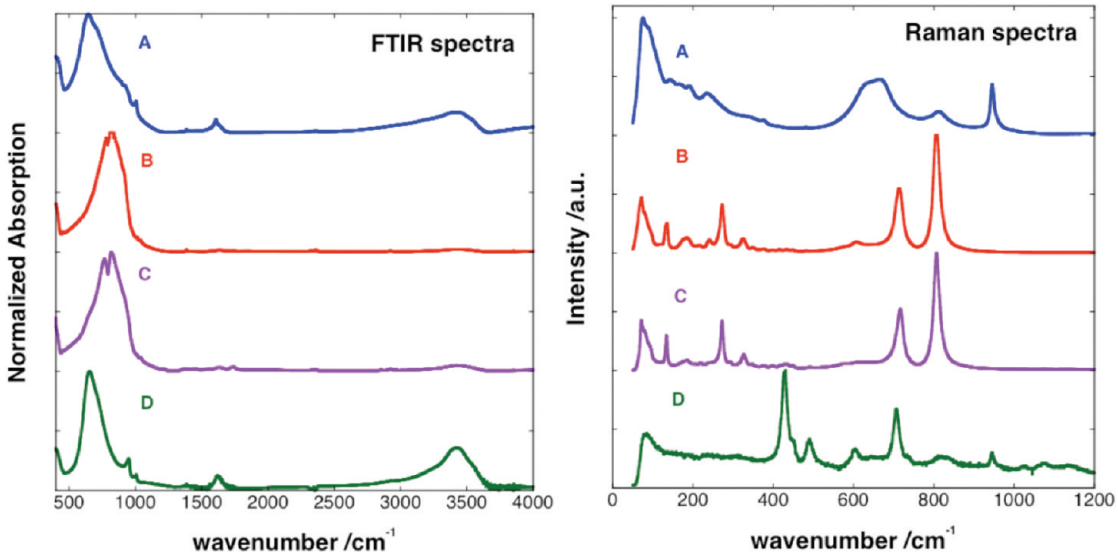

Figure 4. FTIR and Raman spectra of (A) synthesized powder, (B) commercially available WO_3, (C) synthesized powder sintered at 550 °C for 1 h and (D) synthesized powder dispersed in water, followed by 1 week aging and lyophilization in order to obtain.

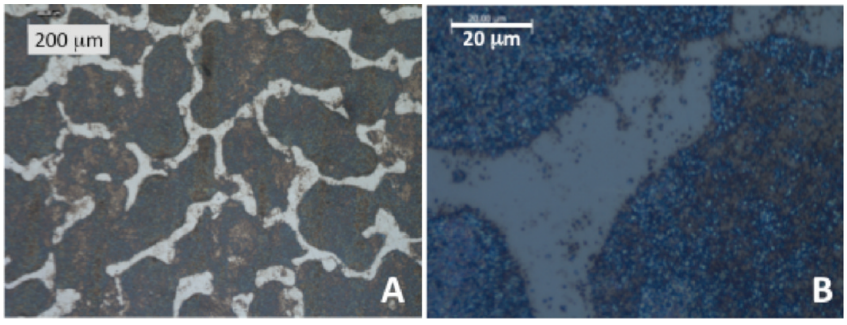

Figure 5. Optical microscope images of a 20 μm drop spacing printed film of tungsten oxide in a PET/ITO substrate, using the Dimatix printer.

which is shifted to lower wavenumbers when the material is in amorphous state rather than in crystalline state.[47] This stretching mode also appears on samples B and C around 710 cm^{-1} (more clear in the Raman spectra). Abroad peak appears at 636 cm^{-1} for powder A only, which is related with O−W−O bending mode for a hydrated sample. This bending mode appears at 328 and 274 cm^{-1} for samples B and C, but in this case without the presence of water molecules. For powder D, the results seem to be between the other samples and are difficult to interpret. All peaks below 200 cm^{-1} observed in powders B and C are attributed to lattice modes of WO_3 crystalline particles.[52] The lattice modes are absent in A and D.

In summary, XRD, FTIR and Raman measurements indicates that powder A has an hydrated hexagonal structure with some amorphous phase, powder B shows a cubic structure, C has a tetragonal structure, and powder D displays an hydrated (more hydrated than powder A) orthorhombic structure also with some amorphous phase.

The coexistence of crystalline/amorphous domains on powders A and D is a result already discussed in the literature.[29] The amount of crystalline/amorphous domains depends of the reaction conditions, such as temperature, pH and concentration. The tungsten oxide produced is also called polycrystalline (a name that can be often misleading because of the presence of an amorphous fraction, see discussion in ref 29); however, such tungsten oxide usually has large fractions of crystalline domains (e.g., 70%, see also ref 29), which does not seem to be the present case since Raman spectra shows mainly amorphous tungsten oxide. Using tungstate acid precursors, Livage et al. studied in great detail the growth mechanism arriving to the conclusion that at high temperatures the water dielectric constant is sufficiently low to increase electrostatic repulsions between W(VI) ions, thus leading to hexagonal phases similar to the one observed in this work with a more open structure.[42] Although the precursor is different, it seems the same mechanism is occurring in this work. The mechanism that leads to orthorhombic structure on powder D is, however, less clear. Probably low temperatures (−30 °C) and/or water sublimation triggers the transition from hexagonal to orthorhombic phase. Also, from the intensity of the W═O Raman peak, it seems the powder D has a larger fraction of crystalline structure, but tungsten oxide is still present in the form of nanoparticles with 200 nm of diameter for this powder.

3.4. Inkjet Printing Characterization. As explained in the experimental section, 20 μm drop spacing was employed in the deposition of tungsten oxide in a PET/ITO substrate, using the Dimatix printer. The images displayed on Figure 5 show optical images of printed films. If no droplet agglomeration took place, a continuous tungsten oxide film would be seen in these images. However, tungsten oxide islands were observed, with a size of approximately 200 μm. The formation of these islands is related with two different factors: agglomeration of deposed droplets due to capillarity effects (the contact angle between

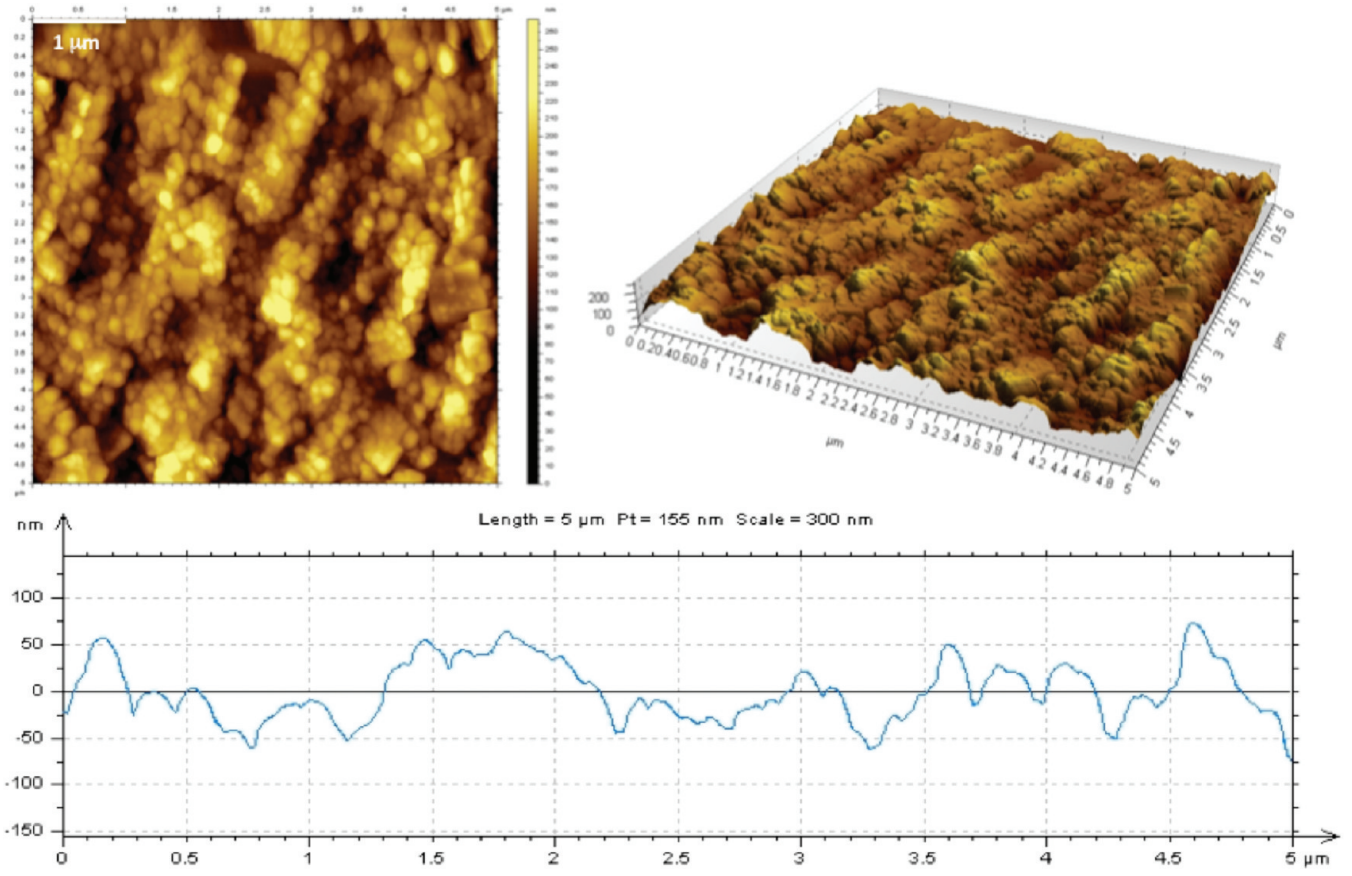

Figure 6. AFM images and rugosity measurements of tungsten oxide printed films on PET/ITO substrates.

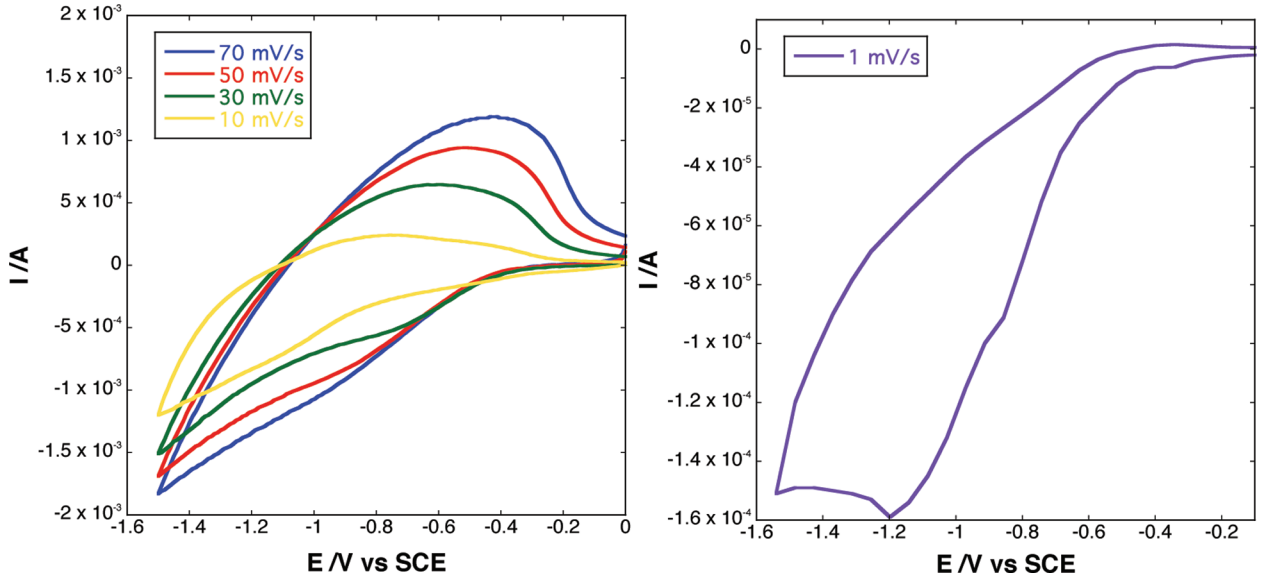

Figure 7. Cyclic voltammogram for the tungsten oxide synthesized nanoparticles measured at several scan rates (left) and cyclic voltammogram with 1 mV s^{-1} scan rate measurement, showing the appearance of the reduction peak (right).

the ink and PET/ITO is 40°), and drying of the droplets, which is not instantaneous.

AFM images displayed on Figure 6 show more details. Tungsten oxide particles are clearly seen, with sizes ranging from 100 to 200 nm in accordance with DLS and sedimentation experiments. The rugosity of the film is also shown on Figure 6, with amplitude of 100 nm for the region investigated. The rugosity of PET/ITO without tungsten oxide particles is much smaller than this (around 5 nm, see Figure S2 in the Supporting Information) showing that this rugosity comes only from the tungsten oxide coating. This is an important aspect for electrochromism, since a higher rugosity leads to a larger interfacial area with the electrolyte layer, thus facilitating Li^+ insertion in the electrochromic material.

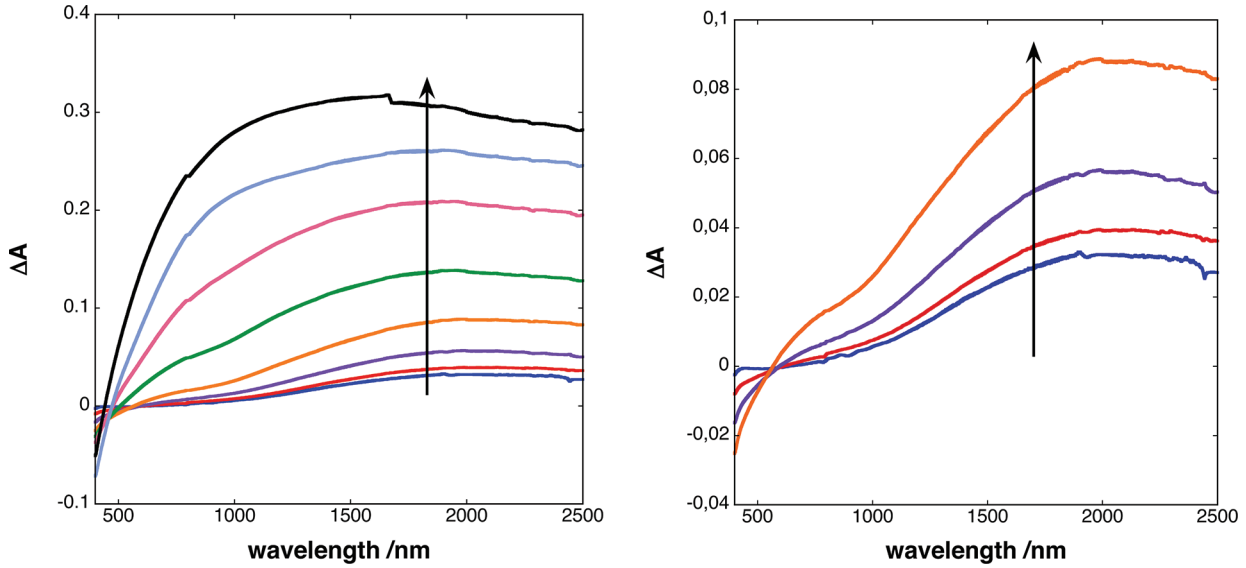

Figure 8. Visible−NIR spectra showing the change in absorbance when a voltage is applied on the device, between the on (i.e., negative voltage, reduced tungsten oxide) and the off (i.e., positive voltage, oxidized tungsten oxide) states at 0.5, 0.7, 0.9, 1.1, 1.3, 1.5, 1.7, and 1.9 V (left) and zoom of the spectra obtained with lower voltages (right).

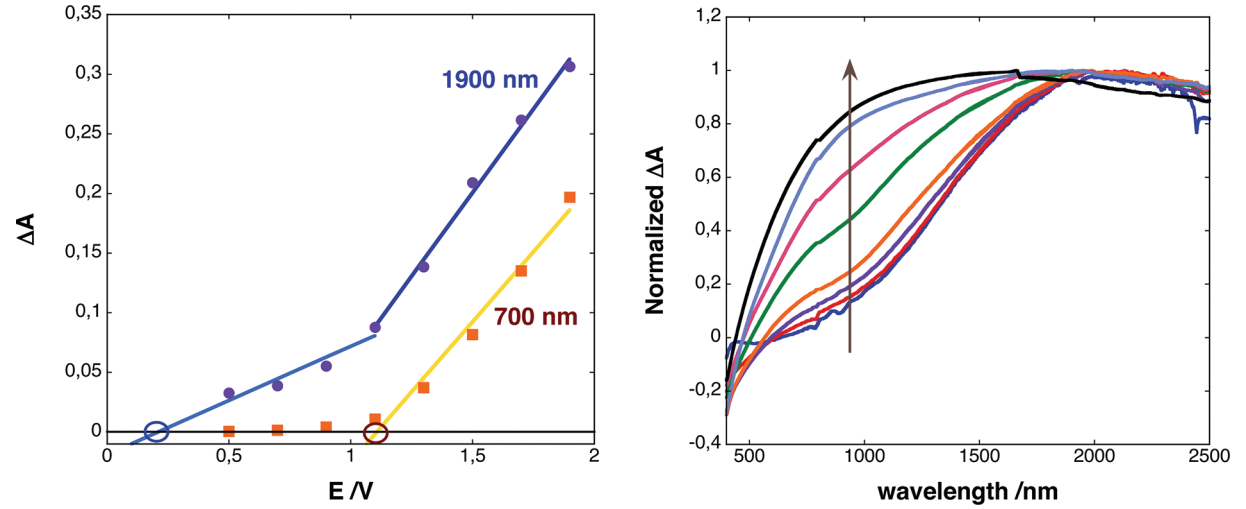

Figure 9. Change of Absorbance plotted against the applied voltage, at 700 and 1900 nm (left) and normalized change of absorbance for 0.5, 0.7, 0.9, 1.1, 1.3, 1.5, 1.7, and 1.9 V (right).

Attempts were made to print powders B and C. However, dispersions with these crystalline powders resulted into particles with sizes too large to pass the filter and, therefore, could not be deposited by inkjet. Such limitation was not observed with D, which could also be deposited by inkjet.

3.5. Electrochemical Characterization. The PET/ITO substrates coated with tungsten oxide nanoparticles by inkjet printing were electrochemically characterized. On Figure 7, a cyclic voltammetry study of such coatings is shown. The results are in accordance with others previously published for tungsten oxide.[46,61] The oxidation wave shows a peak at −0.4 V, but the reduction wave does not show the corresponding reduction peak. This behavior was discussed previously and several explanations were put forward, from which two are described here[62−64] (other explanations are in the review by Monk[29]).

(A) Faughnan and Crandall model (potentiostatic coloration).[17,65] This model relies on two main assumptions: the rate limiting motion is the cation entering the tungsten oxide layer from the electrolyte layer, because a back emf is created at the interface. W(VI) is considered to be the only species existing in the film initially, meaning that cations are absent in the electrochromic layer. The back emf is particularly important in this model, because it explains the absence of a reduction peak.

(B) Ingram, Duffy, and Monk model (electronic percolation threshold)[66]. This model assumes that there is a percolation threshold where below it, the electron motion is the rate limiting step, instead of the cation insertion in model A. Above this threshold, models A and B are similar.

Both models A and B invoke a "characteristic time", which is proportional to the squared film thickness divided by the cation diffusion coefficient. Because of back emf, the response time will exceed this characteristic time. For usual scan rates (50 mV s^{-1}) this implies the absence of the reduction peak, but at smaller scan rates it can appear. To check this aspect, slower scan rates were investigated. Indeed, for 1 mV s^{-1}, a reduction peak was

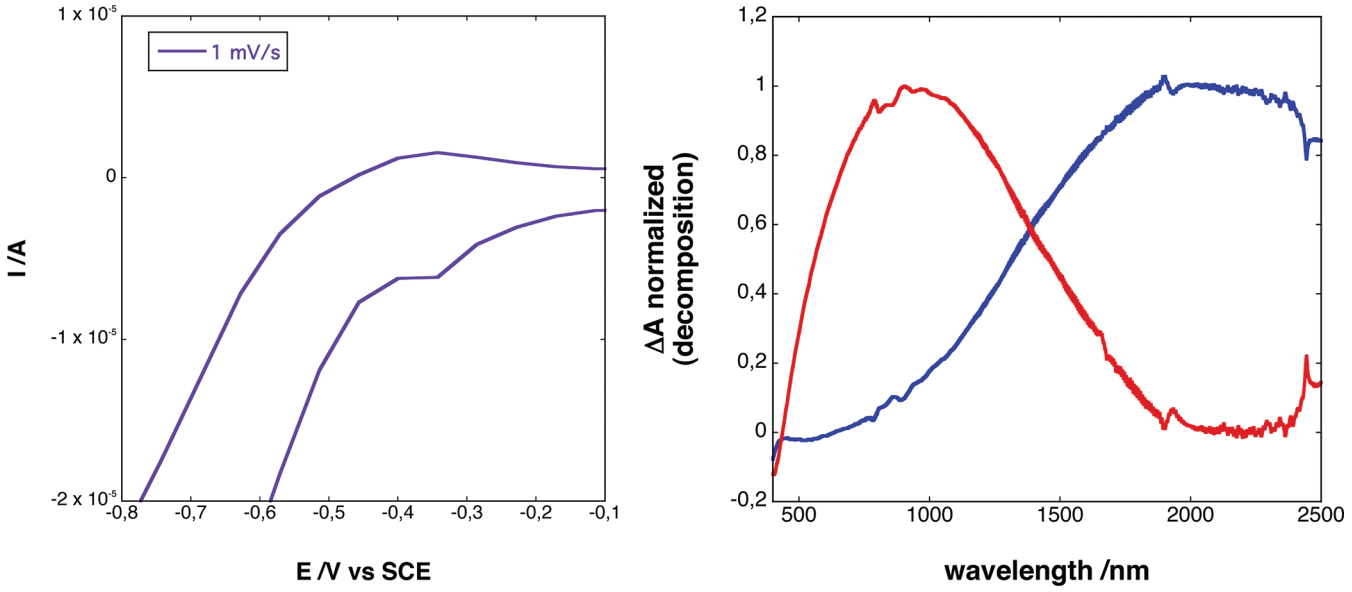

Figure 10. Cyclic voltammogram of 1 mV s^{-1} scan rate measurement zoomed in order to evidence the appearance of a small reduction peak around −0.3 V (left) and decomposition spectra from the normalized change in absorbance to obtain the two theoretical spectra of the two different species (right).

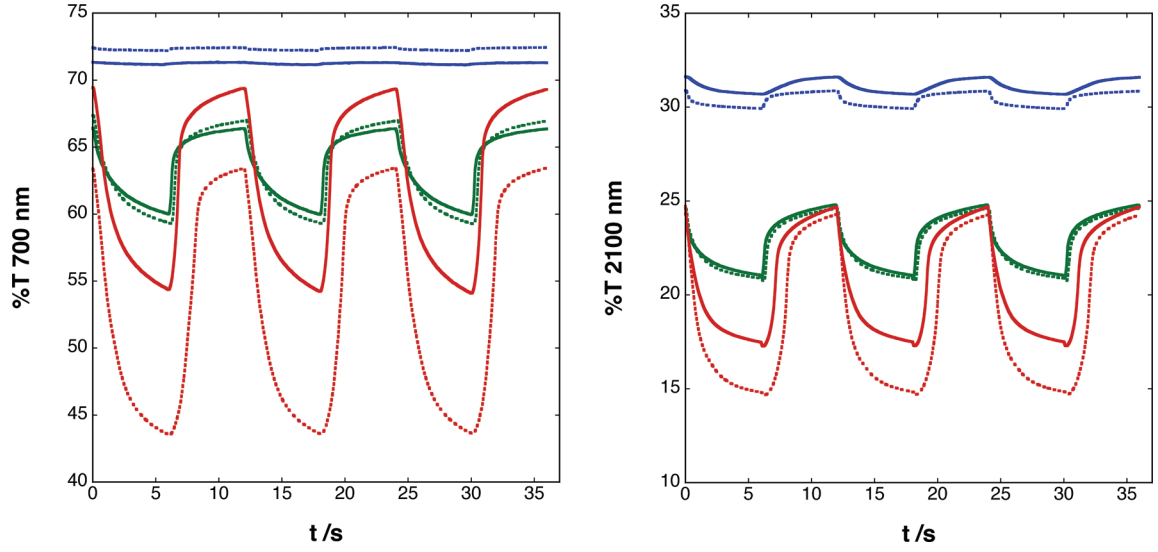

Figure 11. Cycling measurements of electrochromic devices measured at 700 nm (left) and at 2100 nm (right), built with the tungsten oxide printed films with powder A and tested at 0.9 V (blue), 1.5 V (green), and 2 V (red), the straight lines show the initial cycles and the dot lines show the device performance after 1000 cycles.

found at −1.25 V, at the expense of the oxidation peak (Figure 7). A slow scan rate enables Li^+ diffusion to take place, promoting the reduction of the electrochromic film, however the oxidation (accompanied by the exit of the cations from the electrochromic layer) is too fast in comparison with the reduction, so the very well-defined oxidation peak is lost. Figure 7 also shows the decreasing intensity of the oxidation peak with a decreasing scan rate, accompanied by a shift of the peak.

3.6. Vis−NIR Spectroelectrochemistry. The optical properties of the tungsten oxide films were characterized by Vis-NIR spectroelectrochemistry in the wavelength range of 400−2500 nm and voltage range of −2 to 2 V. The measurements were made on a solid-state electrochromic cell, which contained all the components of the device, including the TCO and electrolyte layers. Figure 8 shows the change in absorbance (ΔA) when a voltage is applied on the device, between the on (i.e., negative voltage, reduced tungsten oxide) and the off (i.e., positive voltage, oxidized tungsten oxide) states. Even for low voltages such as −0.5 V, a change of absorbance between on and off states is observed. For voltages below 1.1 V, this response is only active in the NIR portion of the spectra and the absorption spectra peak is around 1900 nm, deep in the NIR region. An isosbestic point is observed at 550 nm, which is indicative of a conversion between two species (Figure 8 (right)).

Above 1.1 V, the peak position shifts to around 1400 nm as the voltage increases, and the visible portion of the spectra becomes active. The isosbestic point disappears, which indicates the presence of a third species (Figure 8 (left)).

dx.doi.org/10.1021/am201606m | ACS Appl. Mater. Interfaces 2012, 4, 1330−1340

Table 2. Electric Current, Transition Time between Colored and Bleached States, Coloration Efficiency, Change in Absorbance and in Transmittance for 0.9, 1.5, and 2 V at 700 and 2100 nm of a Flexible Electrochromic Device Build with the Tungsten Oxide Printed Films on PET/ITO Using Powder A; For Comparison Proposes, Results Obtained with Powder D Are Also Shown

V (V)	wavelength (nm)	Q_c (mC cm^{-2})	Q_b (mC cm^{-2})	$\Delta\%T$	ΔA	CE (cm^2 C^{-1})	τ_c (s)	τ_b (s)
Powder A								
0.9	700	−0.30	0.27	0.7	0.008	29		
1.5	700	−0.90	0.91	12.5	0.034	38	1.7	2.5
2.0	700	−3.0	3.1	26.0	0.090	27	2.0	1.7
0.9	2100	−0.30	0.27	3.9	0.040	133	>6	>6
1.5	2100	−1.00	1.00	12.5	0.092	88	>6	>6
2.0	2100	−2.9	3.1	16.6	0.161	55	2.5	2.4
Powder D								
2.0	700	−2.4	2.3	4.5	0.033	14	>6	>6
2.0	2100	−2.4	2.3	3.1	0.050	22	>6	>6

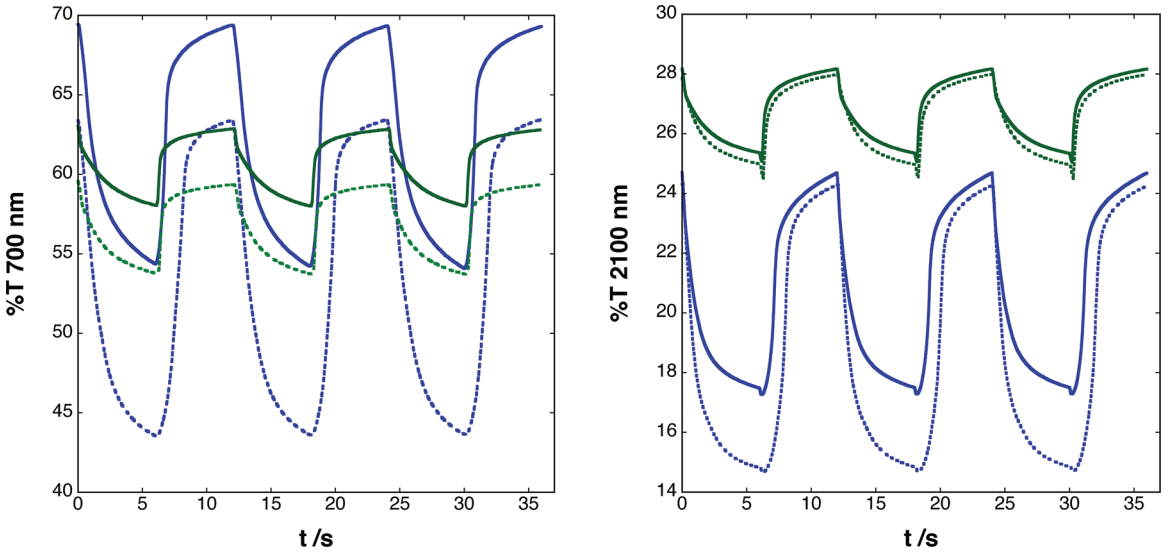

Figure 12. Cycling measurements of electrochromic devices measured at 700 nm (left) and at 2100 nm (right), built with the tungsten oxide printed films with powder A (blue) and powder D (green) and tested at 2 V, the straight lines show the initial cycles and the dot lines show the device performance after 1000 cycles.

This shift is best viewed when the change of absorbance is normalized at the peak (Figure 9). Indeed, for low voltage the optical activity is observed for wavelengths above 1200 nm, while the second component appears with the concomitant shift of the absorption spectra at high voltages. If ΔA is plotted against the applied voltage, at 700 nm the signal only appears above −1.1 V, but at 1900 nm two regimes appear, one above −1.1 V and a second one above −0.3 V (value obtained by extrapolation). The cyclic voltammogram with low scan rate indeed shows a wave at −1.2 V, but it also shows a very small peak around −0.3 V (see Figure 10). These results point out for two different species with different redox potentials and a different absorption spectroscopy.

Different behaviors of the optical absorption for amorphous and polycrystalline WO_3 films were described earlier.[31,35,49,51,67−69] In the case of amorphous WO_3, it was found that the absorption peak is much more shifted into the blue, a result explained because the localization radius of the electron states is much smaller than in a crystalline phase.[68] Small-polaron absorption theory explains this result qualitatively, as described earlier.[22] Alternatively, a theory based on intervalence charge transfer absorption was given even earlier, in which the absorption spectra is caused by charge transfer mechanisms between W(V) and W(VI).[16,24,29] In both cases, although amorphous films are optically active at higher energies (hence, visible range of the spectrum), crystalline states are active in NIR region. This interpretation is in accordance with the data obtained by Raman and XRD spectroscopy (see above), where both amorphous and crystalline (hexagonal) states are observed. So, for low voltage, the hexagonal portion of the WO_3 nanoparticles is being reduced, whereas higher voltages are required for the reduction of the amorphous portion of the nanoparticles.

3.7. Response Time and Cycling. These measurements were done only for inks with powder A and D, because the particles obtained with powder B and C are too large to be printed using inkjet. The device stability was tested by on/off cycling, by alternating between the two states of the device at a given voltage and monitoring the performance at 700 and 2100 nm (see Figure 11). The transmittance contrast for −0.9/+0.9 V cycles is rather small, but for −1.5/+1.5 V cycles the color stability can be measured and is very good after 1000 cycles in both spectral regions, with a slight increase of transmittance contrast after 1000 cycles. The contrast after 1000 cycles improves even more when −2.0/+2.0 V cycles are applied, although the transmittance decreases by about 5% at

700 nm (probably because of electrolyte layer degradation, which causes a yellowing of the device when many cycles are performed). The performance enhancement is much more evident for this case. The reason for this increase of performance in the first 1000 cycles is related with the assembly of the electrochromic cell. W(VI) is present in both electrodes when the device is assembled, and the first cycles establish the electrochemical difference between electrode and counter-electrode that gives rise to the color contrast. Only when W(V) is fully formed in one of the electrodes does the device attain full contrast.

Table 2 shows more details about the electrochromic performance of the device. The coloration time τ_c and bleaching time τ_b were measured, as well as the electric current and the so-called coloration efficiency CE. The coloration/bleaching times, however, are better in the visible region, probably because the amorphous component of the nanoparticles are more accessible for cation insertion. The total electric current Q_c and Q_b are similar for a given voltage, confirming the stability of the assembled devices. A comparison with results obtained for electrochromic devices using powder D is also shown. The performance is much smaller than powder A, as can also be seen on Figure 12. In terms of particle size, both powders are similar, so the main difference lies in the crystalline phase (hexagonal for powder A, orthorhombic for powder D). Therefore these results show that Li^+ insertion in the electrochromic layer is considerably delayed reducing contrast, color efficiency and also coloration and bleaching times, in both visible and NIR regions. Powder D is also more hydrated than powder A (see XRD results), which is also an additional factor that could influence the electrochromic performance. Nevertheless, samples with powder D show the same durability than samples with powder A. In conclusion, these results do not enable a detailed explanation to justify the differences here shown, but they clearly show that powder D is not suitable for this type of devices.

Figure 13 shows photos of the device in on/off states, where the color contrast obtained is best viewed. The device is bendable, without any significant loss of optical activity, and almost completely transparent in the off state. Twenty-five percent loss of absorbance contrast was obtained only after 50000 −2.0/+2.0 V cycles, with 6 s of duration at any wavelength, with very good reproducibility.

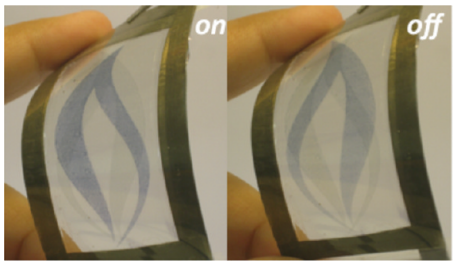

Figure 13. Photos of a flexible electrochromic device built with the tungsten oxide printed films on PET/ITO in on/off states.

4. FINAL COMMENTS

Tungsten oxide nanoparticles sized 200 nm were synthesized via a sol−gel method. An inkjet formulation of these nanoparticles is proposed, which was deposited on the surface of flexible and heat sensitive PET/ITO electrode. The hydrated nanoparticles have simultaneously amorphous and crystalline (hexagonal) states. It is demonstrated that such tungsten oxide coatings have electrochromic activity with a good color contrast. Spectrolectrochemical measurements evidenced a dual response in the visible and the NIR part of the spectrum, depending on the applied voltage. Such behavior is connected to the presence of amorphous and crystalline states on the nanoparticles, and might be used in the future to construct devices in which light can be filtered on the NIR or NIR/visible regions, by controlling the applied voltage. We therefore propose the exploration of this phenomenon in applications such as electrochromic windows, which would allow the entrance of sun visible light while filtering the NIR part of the spectrum at low voltages. The application on flexible substrates can be useful too, in which NIR contrast might, for example, be used in the future for displaying hidden messages in reversible (on/off) NIR spectral tags for markerless identification applications.[70] Future synthesis efforts will be crucial for possible commercial applications of this technology, in order to obtain even better contrast at low voltage in the NIR region of the spectra.

■ ASSOCIATED CONTENT

Supporting Information

Sedimentation velocity of ink formulations, differential scanning calorimetry of tungsten oxide samples, and rugosity measurement of ITO/PET substrate (PDF). This material is available free of charge via the Internet at http://pubs.acs.org.

■ AUTHOR INFORMATION

Corresponding Author

*Tel.: + 351 212948355; Fax: + 351 212948385. E-mail: catl@fct.unl.pt.

Notes

The authors declare no competing financial interest.

■ ACKNOWLEDGMENTS

This work has been supported by Fundação para a Ciência e a Tecnologia through Grant PEst-C/EQB/LA0006/2011. Financial support from Fundação para a Ciência e a Tecnologia (FCT-MCTES) (project PTDC/QUI/67786/2006) and QREN-SI I&DT Co-Promoção - Project Yinvisible pré-industrialização (n° 3498) are acknowledged. CP and CC acknowledge FCT-MCTES and YDreams for PhD grants (SFRH/BDE/15563/2005 and SFRH/BDE/33291/2008 respectively). CENTI − Centre for Nanotechnology and Smart Materials, is acknowledged for the DSC and TGA measurements. The Restoration and Conservation Department at Faculdade de Ciências e Tecnologia is acknowledged for the FTIR, Raman Spectroscopy and X-ray Fluorescence equipments used in the characterization measurements. Dr. Graça Soveral and Ms. A.P. Martins at REQUIMTE, Chemistry Department of Faculdade de Ciências e Tecnologia, are acknowledged for DLS measurements.

■ REFERENCES

(1) Nathan, A.; Chalamala, B. R. *Proc. IEEE* **2005**, *93*, 1235−1238.
(2) Yan, H.; Chen, Z.; Zheng, Y.; Newman, C.; Quinn, J. R.; Dotz, F.; Kastler, M.; Facchetti, A. *Nature* **2009**, *457*, 679−686.
(3) Bharathan, J.; Yang, Y. *Appl. Phys. Lett.* **1998**, *72*, 2660−2662.
(4) Andersson, P.; Forchheimer, R.; Tehrani, P.; Berggren, M. *Adv. Funct. Mater.* **2007**, *17*, 3074−3082.

(5) Huang, D.; Liao, F.; Molesa, S.; Redinger, D.; Subramanian, V. *J. Electrochem. Soc.* **2003**, *150*, G412−G417.
(6) Lee, H. H.; Chou, K. S.; Huang, K. C. *Nanotechnology* **2005**, *16*, 2436−2441.
(7) Small, W. R.; Masdarolomoor, F.; Wallace, G. G.; Panhuis, M. *J. Mater. Chem.* **2007**, *17*, 4359−4361.
(8) Cranton, W. M.; Wilson, S. L.; Ranson, R.; Koutsogeorgis, D. C.; Chi, K.; Hedgley, R.; Scott, J.; Lipiec, S.; Spiller, A.; Speakman, S. *Thin Solid Films* **2007**, *515*, 8534−8538.
(9) Van Osch, T. H. J.; Perelaer, J.; de Laat, A. W. M.; Schubert, U. S. *Adv. Mater.* **2008**, *20*, 343−345.
(10) Shim, G. H.; Han, M. G.; Sharp-Norton, J. C.; Creager, S. E.; Foulger, S. H. *J. Mater. Chem.* **2008**, *18*, 594−601.
(11) Sekitani, T.; Noguchi, Y.; Zschieschang, U.; Klauk, H.; Someya, T. *P. Natl. Acad. Sci. U.S.A.* **2008**, *105*, 4976−4980.
(12) Kim, D.; Jeong, Y.; Song, K.; Park, S. K.; Cao, G.; Moon, J. *Langmuir* **2009**, *25*, 11149−11154.
(13) Monk, P. M. S.; Mortimer, R. J.; Rosseinsky, D. R. *Electrochromism and Electrochromic Devices*; Cambridge University Press: Cambridge, U.K., 2007.
(14) (a) Pinheiro, C.; Parola, A. J.; Pina, F.; Laia, C. A. T. *Electrochim. Acta* **2009**, *54*, 5593−5597. (b) Pinheiro, C.; Parola, A. J.; Laia, C. A. T.; Camara, A.; Pina, F. *New J. Chem.* **2009**, *33*, 2144−2147.
(15) Beaujuge, P. M.; Reynolds, J. R. *Chem. Rev.* **2010**, *110*, 268−320.
(16) Granqvist, C. G. *Handbook Of Inorganic Electrochromic Materials*; Elsevier: Dordrecht, The Netherlands, 2002.
(17) Faughnan, B. W.; Crandall, R. S.; Heyman, P. M. *RCA Rev.* **1975**, *36*, 177−197.
(18) Granqvist, C. G. *Sol. Energy Mater. Sol. Cells* **2000**, *60*, 201−262.
(19) Granqvist, C. G.; Green, S.; Niklasson, G. A.; Mlyuka, N. R.; von Kraemer, S.; Georen, P. *Thin Solid Films* **2010**, *518*, 3046−3053.
(20) Rauh, R. D. *Electrochim. Acta* **1999**, *44*, 3165−3176.
(21) Livage, J.; Ganguli, D. *Sol. Energy Mater Sol. Cells* **2001**, *68*, 365−381.
(22) Niklasson, G. A.; Granqvist, C. G. *J. Mater. Chem.* **2007**, *17*, 127−156.
(23) Baetens, R.; Jelle, B. P.; Gustavsen, A. *Sol. Energy Mater. Sol. Cells* **2010**, *94*, 87−105.
(24) Crandall, R. S.; Faughnan, B. W. *Appl. Phys. Lett.* **1976**, *28*, 95−97.
(25) Zeller, H. R.; Beyeler, H. U. *Appl. Phys.* **1977**, *13*, 231−237.
(26) Hashimoto, S.; Matsuoka, H. *J. Electrochem. Soc.* **1991**, *138*, 2403−2408.
(27) Batchelor, R. A.; Burdis, M. S.; Siddle, J. R. *J. Electrochem. Soc.* **1996**, *143*, 1050−1055.
(28) Lee, S. H.; Cheong, H. M.; Tracy, C. E.; Mascarenhas, A.; Czanderna, A. W.; Deb, S. K. *Appl. Phys. Lett.* **1999**, *75*, 1541−1543.
(29) Monk, P. M. S. *Crit. Revs. Solid State Mater. Sci.* **1999**, *24*, 193−226.
(30) Lee, S. H.; Cheong, H. M.; Zhang, J. G.; Mascarenhas, A.; Benson, D. K.; Deb, S. K. *Appl. Phys. Lett.* **1999**, *74*, 242−244.
(31) Berggren, L.; Azens, A.; Niklasson, G. A. *J. Appl. Phys.* **2001**, *90*, 1860−1863.
(32) Granqvist, C. G.; Avendano, E.; Azens, A. *Thin Solid Films* **2003**, *442*, 201−211.
(33) Azens, A.; Gustavsson, G.; Karmhag, R.; Granqvist, C. G. *Solid State Ionics* **2003**, *165*, 1−5.
(34) Ho, J. J.; Chen, C. Y.; Lee, W. J. *Electron. Lett.* **2004**, *40*, 510−511.
(35) Kamal, H.; Akl, A. A.; Abdel-Hady, K. *Physica B* **2004**, *349*, 192−205.
(36) Rodrigues, L. C.; Barbosa, P. C.; Silva, M. M.; Smith, M. J.; Goncalves, A.; Fortunato, E. *Opt. Mater.* **2009**, *31*, 1467−1471.
(37) Silva, M. M.; Barbosa, P. C.; Rodrigues, L. C.; Goncalves, A.; Costa, C.; Fortunato, E. *Opt. Mater.* **2010**, *32*, 719−722.
(38) Vemuri, R. S.; Bharathi, K. K.; Gullapalli, S. K.; Ramana, C. V. *ACS Appl. Mater. Interfaces* **2010**, *2*, 2623−2628.
(39) Gullapalli, S. K.; Vemuri, R. S.; Ramana, C. V. *Appl. Phys. Lett.* **2010**, *96*, 171903.
(40) Okamoto, H.; Ishikawa, A.; Kudo, T. *Bull. Chem. Soc. Jpn.* **1989**, *62*, 2723−2724.
(41) Judeinstein, P.; Livage, J. *J. Mater. Chem.* **1991**, *1*, 621−627.
(42) Livage, J.; Guzman, G. *Solid State Ionics* **1996**, *84*, 205−211.
(43) Lee, K. D. *Thin Solid Films* **1997**, *302*, 84−88.
(44) Ozer, N.; Lampert, C. M. *Sol. Energy Mater. Sol. Cells* **1998**, *54*, 147−156.
(45) Santato, C.; Odziemkowski, M.; Ulmann, M.; Augustynski, J. *J. Am. Chem. Soc.* **2001**, *123*, 10639−10649.
(46) Ozkan, E.; Lee, S. H.; Liu, P.; Tracy, C. E.; Tepehan, F. Z.; Pitts, J. R.; Deb, S. K. *Solid State Ionics* **2002**, *149*, 139−146.
(47) Badilescu, S.; Ashrit, P. V. *Solid State Ionics* **2003**, *158*, 187−197.
(48) Brezesinski, T.; Fattakhova-Rohlfing, D.; Sallard, S.; Antonietti, M.; Smarsly, B. M. *Small* **2006**, *2*, 1203−1211.
(49) Deepa, M.; Srivastava, A. K.; Kar, M.; Agnihotry, S. A. *J. Phys. D. Appl. Phys.* **2006**, *39*, 1885−1893.
(50) Deepa, M.; Joshi, A. G.; Srivastava, A. K.; Shivaprasad, S. M.; Agnihotry, S. A. *J. Electrochem. Soc.* **2006**, *153*, C365−C376.
(51) Deepa, M.; Singh, D. P.; Shivaprasad, S. M.; Agnihotry, S. A. *Curr. Appl. Phys.* **2007**, *7*, 220−229.
(52) Djaoued, Y.; Priya, S.; Balaji, S. *J. Non-Cryst. Solids* **2008**, *354*, 673−679.
(53) Wang, W.; Pang, Y.; Hodgson, S. N. B. *Microporous Mesoporous Mater.* **2009**, *121*, 121−128.
(54) Balaji, S.; Djaoued, Y.; Albert, A. S.; Bruening, R.; Beaudoin, N.; Robichaud, J. *J. Mater. Chem.* **2011**, *21*, 3940−3948.
(55) Laia, C. A. T.; López-Cornejo, P.; Costa, S. M. B.; D'Oliveira, J.; Martinho, J. M. G. *Langmuir* **1998**, *14*, 3531−3537.
(56) Petzold, G.; Goltzsche, C.; Mende, M.; Schwarz, S.; Jaeger, W. *J. Appl. Polym. Sci.* **2009**, *114*, 696−704.
(57) Detloff, T.; Sobisch, T.; Lerche, D. *Powder Technology* **2007**, *174*, 50−55.
(58) DMP-2800 Materials Printer User Manual, Dimatix.
(59) Daniel, M. F.; Desbat, B.; Lassegues, J. C.; Gerand, B.; Figlarz, M. *J. Solid State Chem.* **1987**, *67*, 235−247.
(60) Baserga, A.; Russo, V.; Di Fonzo, F.; Bailini, A.; Cattaneo, D.; Casari, C. S.; Li Bassi, A.; Bottani, C. E. *Thin Solid Films* **2007**, *515*, 6465−6469.
(61) Pecquenard, B.; Lecacheux, H.; Garcia, S. C.; Livage, J. *J. Sol−Gel Sci. Technol.* **1998**, *13*, 923−927.
(62) Green, M.; Smith, W. C.; Weiner, J. *Thin Solid Films* **1976**, *38*, 89−100.
(63) Zhang, J. G.; Benson, D. K.; Tracey, C. E.; Deb, S. K.; Czanderna, A. W.; Bechinger, C. *J. Electrochem. Soc.* **1997**, *144*, 2022−2026.
(64) Zhang, L.; Goto, K. S. *Proc. Electrochem. Soc* **1990**, *90−2*, 23−29.
(65) Faughnan, B. W.; Crandall, R. S. *Display Devices*; Springer-Verlag: Berlin, 1980.
(66) Ingram, M. D.; Duffy, J. A.; Monk, P. M. S. *J. Electroanal. Chem.* **1995**, *380*, 77−82.
(67) Bessiere, A.; Marcel, C.; Morcrette, M.; Tarascon, J. M.; Lucas, V.; Viana, B.; Baffier, N. *J. Appl. Phys.* **2002**, *91*, 1589−1594.
(68) Niklasson, G. A.; Berggren, L.; Larsson, A. L. *Sol. Energy Mater. Sol. Cells* **2004**, *84*, 315−328.
(69) Ederth, J.; Hoel, A.; Niklasson, G. A.; Granqvist, C. G. *J. Appl. Phys.* **2004**, *96*, 5722−5726.
(70) Azuma, R.; Baillot, Y.; Behringer, R.; Feiner, S.; Julier, S.; MacIntyre, B. *IEEE Comput. Graph.* **2001**, *21*, 34−47.